COBEM 2021 26th International Congress of Mechanical Engineering
ABCM Associação Brasileira de Engenharia e Ciências Mecânicas
November 22-26, 2021, Virtual Congress, Brazil

COB-2021-0874
EXPERIMENTAL AND NUMERICAL EVALUATION OF AN IN-FLIGHT ANGLE OF ATTACK MEASUREMENT SYSTEM FOR HIGH POWER MODEL ROCKETS

Caio Dias Fernandes
Bruna Hartmann Coutinho
Breno Foltran Borges
Bruno Hashinokuti Iwamoto
Dimitri Zuave Costa da Silva
Luiz Paulo Baldo Braun
William Rodrigo Lüdtke
Amir Antônio Martins de Oliveira Jr
Universidade Federal de Santa Catarina (UFSC), Department of Mechanical Engineering
Apex Rocketry, 88040-900. Florianópolis / SC, Brazil
caio.diasfernandes@gmail.com; brunahcoutinho@gmail.com; breno.tibagi@gmail.com; iwamoto.bruno@gmail.com; dimitrizuave14@gmail.com; luizpbraun@gmail.com; williamr.ludtke@gmail.com; amir.oliveira@gmail.com

Abstract. *The angle of attack (α) affects the drag, flight path, and flight stability during rocket ascent. This work proposes an in-flight α measurement system based on pressure measurements at the surface of the nosecone for low apogee rockets. An electronic micro differential pressure transducer was selected to measure the pressure difference between selected points in the rocket's nosecone. Wind tunnel tests were performed to correlate the α with the sensor output at low Mach numbers ($M_a \simeq 0.08$). The experimental results were further used as a reference for the construction of CFD models of the external flow in the rocket's nosecone with the aim of predicting the measurements in an extended Mach number range (up to $M_a \simeq 0.7$). The numerical results allowed for an extended model correlating α with the differential pressure transducer output (C_h). The estimate of model's errors completes the analysis.*

Keywords: *aerodynamics, high power rocketry, wind tunnel, CFD.*

1. INTRODUCTION

The multidisciplinary engineering field of high power model rocketry mainly consists on designing low apogee, single stage, passively-controlled rockets to be flown in varied missions proposed by aerospace design competitions. This work evaluates a technology demonstration payload to be carried in a model rocket - developed by Apex Rocketry for its Armação-A22 rocket (depicted in Fig. 1) - whose principal objective is measuring a rocket's angle of attack (α) during flight.

The angle of attack is defined as the angle between the rocket's longitudinal axis and its resultant velocity vector. In situations where there is no ambient wind (atmospheric perturbations) α tends towards zero, indicating that the rocket's velocity vector is aligned with its instantaneous trajectory. In most flight scenarios, however, there are considerable amounts of atmospheric perturbations, resulting in larger values of α. This situation is especially evident when the rocket is subjected to lateral wind gusts, when it performs quick maneuvers (for actively controlled rockets), or as the rocket exits its launch pad during launch procedures. In terms of flight dynamics, α is a crucial metric in assessing the stability of a flight vehicle, and both classical model rocketry literature (Barrowman and Barrowman (1966)) and modern rocket flight trajectory modeling software (Box *et al.* (2010)) preoccupy themselves with estimating the magnitude and frequency of oscillations of α, in order to carry out aerodynamic and stability calculations.

Common telemetry avionics often include chip-sets capable of measuring a rocket's speed and orientation, such as the standard IMU (inertial measurement units) sensors found in most modern smartphones. However, these gyroscopic and accelerometer based sensors are not capable of measuring α. Mitchell and Peck (1955) developed an α measurement system, that was tested and calibrated in a wind tunnel in order to establish the corrections that needed to be applied to the measured in-flight data. More recently, Pavliuchenko *et al.* (2020) measured the angle of attack of an Aerophysical Missile Complex using a Hall effect sensor, in order to study its oscillations and relate it with flight stability. This work proposes an in-flight α measurement system based on pressure measurements at the surface of the rocket's nosecone.

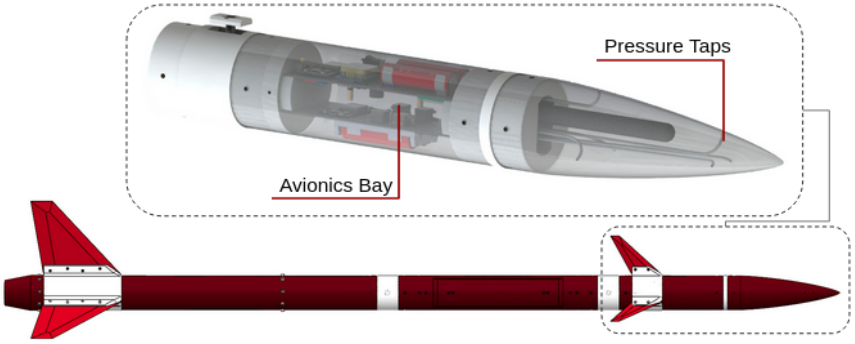

Figure 1: Depiction of the angle of attack measurement payload mounted on the Armação rocket's nosecone.

When flying at an angle of attack, a non-uniform pressure field is developed along the rocket's nosecone surface. As a result, a distinctive pressure difference can be observed at opposite sides of the nosecone. The proposed α measurement system captures this pressure gradient through the use of electronic micro differential pressure transducers.

Avelar *et al.* (2014) analyzed the boundary layer of a rocket nosecone during transonic regime through wind tunnel testing with pressure sensitive paint (PSP) and pressure taps, and compared the experimental results with CFD simulations. They obtained a good agreement between experimental and numerical results, even though they neglected the effects of the wind tunnel's walls in the simulations. Nakakita *et al.* (2012) also performed a comparison between experimental wind tunnel pressure data, obtained through PSP and pressure transducers, and CFD simulations. The experimental results were all in accordance with themselves and with the numerical results, validating therefore the CFD analysis.

Following similar research objectives to the aforementioned works, this work aims to combine wind tunnel and CFD data to develop a transfer model correlating the differential pressure readings acquired by the proposed in-flight α measurement system with the rocket's actual angle of attack, seeking to determine by how much and how often the rocket deviates from nominal flight conditions. Wind tunnel tests have been carried out at low Mach numbers (M_a) with a model nosecone equipped with the previously described micro electronic differential pressure transducers. Water-column manometer pressure readings were also obtained during said testing. These experimental results were used as the basis of reference for a computational fluid dynamics (CFD) study of the model rocket in free-flight at various α and M_a scenarios. The numerical results were then used to develop and expand the transfer model for an extended range of flight conditions. Finally, comparisons between the CFD and experimental results were used to estimate an uncertainty range for the complete transfer model. Due to Covid-19 restrictions, real flight data is not currently available for analysis.

2. METHODOLOGY

2.1 System architecture and experimental setup

The angle of attack in-flight measurement system developed by Coutinho (2021) and further evaluated in this work uses a micro electronic differential pressure transducer to capture the local instantaneous total pressure along selected measurement points in the rocket's nosecone. The MPXV7002DP differential pressure transducer from NXP Semiconductors was selected (Fig. 2b), due to its sufficient measurement range and availability. Pressure readings are obtained in three symmetric locations separated by 120° and located at the same lengthwise position along the rocket's nosecone surface, as depicted in Fig. 3a. The differential pressure sensor is then wired with one of the aforementioned pressure readings acting as the reference value.

In her thesis, Coutinho (2021) also described a set of wind tunnel tests to measure the pressure differences of the rocket's nosecone for various angles of attack. The goal was to acquire baseline measurements to validate the proposed system architecture. Throughout the wind tunnel tests, data was obtained from two different sources of measurement, a water-column manometer and the previously described differential pressure sensor system configuration.

A model nosecone prototype was constructed and three rows of ten evenly spaced pressure taps were drilled in its surface, separated by 120° along the nosecone's circumference. For clarity, these rows are referred throughout this work as measurement lines A, B and C, with Arabic numerals describing the pressure taps (as shown in Fig. 2a). The experimental setup of the wind tunnel tests with this model nosecone is shown in Fig. 3. Copper capillary tubes were internally affixed to the drilled pressure taps, and capillary silicon hoses were used to connect these tubes with the manometer and the sensor.

All of the wind tunnel tests were performed with a speed of 26.2 m/s. This speed corresponded to the maximum safe operating condition for the subsonic wind tunnel available at UFSC. The tests were carried out for $\alpha = [0°, 5°, 10°]$, and in all experimental conditions the measurement line A was vertically aligned and was taken as the reference, with

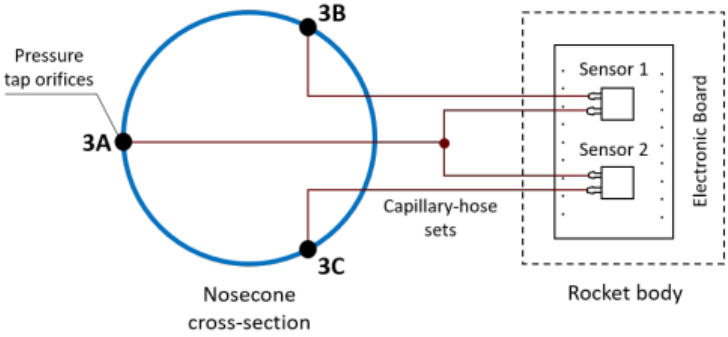

(a) Scheme of sensor system set-up proposed for third orifices as an example. Source: Coutinho (2021).

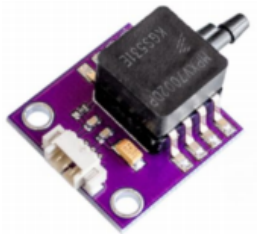

(b) Pressure Transducer. Source: NXP (2017).

Figure 2: Sensor system electronic set scheme with pressure transducer in evidence.

lines B and C being symmetrically opposed to line A. Moreover, in the wind tunnel experiments the on-coming wind hit line A directly (the nosecone was pitched downwards), leading to positive pressure values in this line. For clarity, this condition will be referenced as a positive angle of attack ($\alpha > 0$) throughout this work, with the opposite loading condition (nosecone pitched up) being a negative angle of attack ($\alpha < 0$).

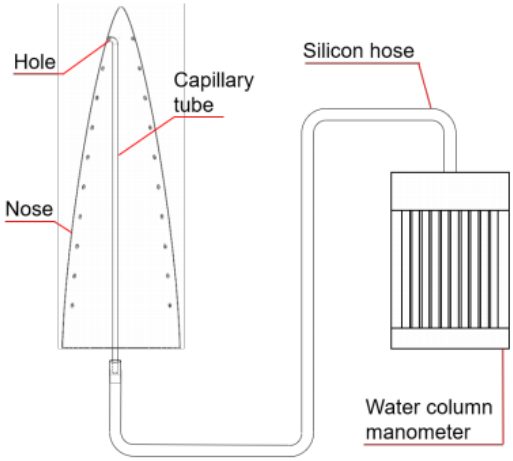

(a) Scheme of 1 of 30 hole-capillary-hose experimental setup connected to the water column manometer. Elements out of scale. Source: Coutinho (2021).

(b) Experimental setup at wind tunnel with manometer installed. Source: Coutinho (2021).

Figure 3: Experimental scheme and set-up of nosecone prototype inside the wind tunnel.

The sequence of wind tunnel experiments was performed in three stages. Firstly, baseline values for all pressure taps were obtained using only the manometer. Secondly, only the sensor was used to acquire differential pressure readings for the third and ninth pressure taps. Lastly, a Y-connector divided the hoses into two exits, the manometer's and the sensors', in order to compare both measurements in real time for the third and ninth pressure taps.

Both measurements methods were capable of distinctively capturing the pressure differences along the different measurement lines, indicating that the proposed system architecture for the differential pressure transducer could potentially be used to estimate the rocket's angle of attack. This work will focus on the last experimental results obtained, comparing the manometer and sensor system, but further results are presented and discussed in Coutinho (2021).

2.2 Computational fluid dynamics

Apex Rocketry's Armação rocket - as well as most other low apogee high power rocket designs - is designed to reach top speeds in the transonic regime, namely attaining $M_a = 0.7$ (roughly 860 km/h) when the rocket stops accelerating after the propellant burnout. As previously discussed, the experimental facilities at UFSC only allowed for wind tunnel testing at low speeds (Mach numbers of roughly 0.08). To evaluate the proposed angle of attack measurement system at higher speeds, ANSYS Fluent v.20 was used to create different RANS (Reynolds Averaged Navier Stokes) CFD setups so as to numerically model the rocket at $M_a = [0.08, 0.4, 0.7]$ and $\alpha = [0°, \pm 2.5°, \pm 5°, \pm 7.5°, \pm 10°]$. Larger magnitudes of α were not considered given the difficulties of modeling detached boundary layer flows with RANS formulations.

Figure 4 illustrates the fluid domain of the numerical model. It consists of a simplified version of the Armação rocket only including its nosecone and fuselage. This was done to avoid large regions of detached, re-circulating flow, that would occur behind the nosecone in case the adjacent body tube was not present. The rocket's stabilizing fins and canards were omitted to avoid geometrical complexity during meshing, considering that their effect on the nosecone's pressure field was negligible. Surface probes were placed at the pressure taps locations to record the numerical total pressure values at these points. The rocket's simplified body is surrounded by a large, cylindrical fluid domain, with dimensions following the recommendations cited in Nakos (2013).

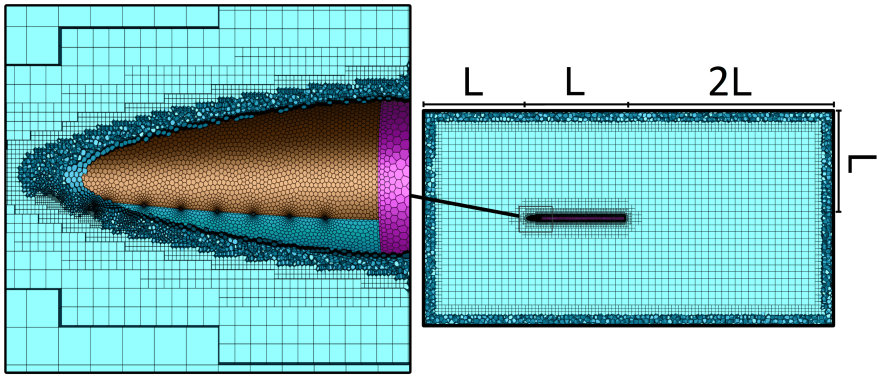

Figure 4: Fluid domain proportions and computational mesh, highlighting the boundary layer on the nosecone. L denotes the total length of the rocket geometry.

An unstructured, hybrid meshing approach was employed to discretize the fluid domain using large hexahedral elements in regions far form the nosecone's surface, and fine polyhedral elements in the near-wall flow region. Such hybrid-element meshing approaches combine the benefits of structured grids (providing more stable results outside of the boundary layer region) and unstructured grids (better conformation to geometry at the boundary region). This approach has been shown to provide good results for external aerodynamics (Zore *et al.*, 2019) and is a standard feature of recent ANSYS Fluent releases. Fig. 4 showcases the meshed domain.

A tri-dimensional, steady state, fully turbulent, RANS CFD formulation was adopted for all of the M_a and α scenarios considered in this work. All of the cases were also modeled using pressure-based solvers, and with second order upwind discretization schemes for all of the modeled equations. Apart from the aforementioned physical and numerical considerations, the developed CFD models have distinct setups for the incompressible ($M_a = 0.08$) and compressible ($M_a = [0.4, 0.7]$) flow regimens.

For the incompressible cases, air with standard constant thermo-physical properties at sea-level pressure was considered as the working fluid. Velocity inlet and pressure outlet boundary conditions were adopted at the fluid domain's far-field, following guidelines presented in Goetten *et al.* (2019) . The SIMPLE (Semi-Implicit Method for Pressure Linked Equations) solution method using the pressure-based segregated solver was implemented for the $M_a = 0.08$ cases, with pressure and momentum relaxation factors of 0.3 and 0.7, respectively.

For the compressible cases, the air's density (ρ) and kinematic viscosity (ν) were modeled following the ideal gas law and the Sutherland law, respectively. Pressure far-field boundary conditions were imposed at all of the domain's frontiers, following recommendations in Mueller *et al.* (2020). A pseudo-transient coupled momentum-continuity algorithm based on the pressure-based coupled solver was used. This method solves the momentum and mass conservation equations simultaneously, and is often recommended for compressible aerodynamic applications as mentioned in Honório and Maliska (2014). Given the flow's compressible nature for the $M_a = [0.4, 0.7]$ cases, the energy equation was also included to the Reynolds-averaged Navier-Stokes equations. Under-relaxation factors of 0.5, 0.5, and 0.75 were used for the pressure, momentum, and energy equations, respectively.

The $k\omega$ SST (Menter *et al.*, 2003) and the Spallart-Allmaras (SA) (Spalart and Allmaras, 1992) turbulence models were employed to estimate the turbulent fluctuations of the RANS equations for the previously described CFD model setups. These turbulent models are amply referenced in literature as good closure models for fully developed turbulent flows in external aerodynamic applications (Goetten *et al.*, 2019).

A mesh independence study was carried out for both turbulence models considering a worst case scenario of $\alpha = -10°$ and $M_a = 0.7$, where the largest pressure gradients and shear stresses at the rocket's nosecone are expected to occur. Figure 5 illustrates the results of this analysis. Three levels of surface geometry and boundary layer refinement

were evaluated. Two criteria were selected to evaluated mesh independence, the mean coefficient of pressure along the measurement lines ($\overline{C_p}$), and the mean coefficient of differential pressure ($\overline{C_h}$), both of which are non-dimensional flow coefficients detailed in Section 2.3. Following this analysis, a meshing setup with approximately 602 thousand total cells was selected. This setup also showed average $y+$ values ranging from 1.5 to 3.1, indicating that the mesh is suitable for the selected turbulence models. The $k\omega$ SST turbulence model showed better residual convergence during preliminary testing, and was therefore selected for the rest of the CFD simulations.

The results presented continuity residuals convergence in the order of 1e-02, while k and ω residuals converged in the order of 1e-04. Velocity components residuals converged in the order of 1e-06 after 100 iterations and pressure monitors were also applied in the pressure taps regions to ensure its stabilization through the iterations. Finally, since the shape of the nosecone is axisymmetric on the z-axis, force monitors were applied to confirm the resulting force on the z-direction is zero, while values on x-direction and y-direction are proportional to drag and lift, respectively.

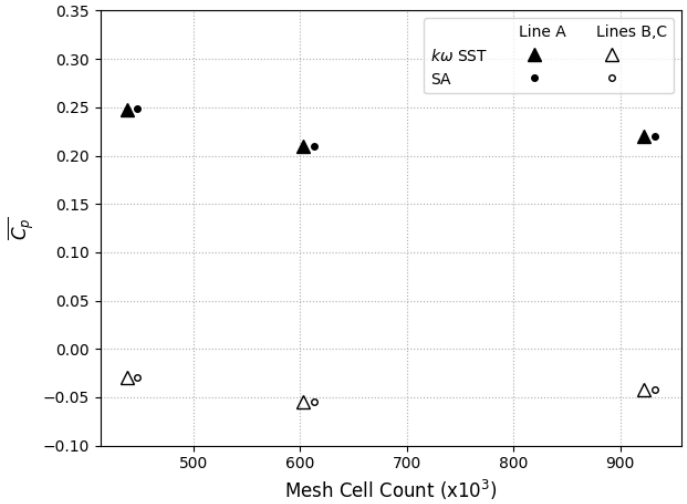

Figure 5: Mesh and turbulence model independence analysis. SA meshes have the same cell count as $k\omega$ SST meshes, but were slightly shifted for ease of visualization. Values for lines B and C correspond to the combined average of these lines.

2.3 Transfer model

The main objective of this work is combining the available experimental and numerical data in order to correlate the in-flight measurements with real values of α; and, in so doing, designing a method for estimating how much and how often the rocket deviates from nominal conditions during flight. Combining numerical and experimental data points is a common goal during the design optimization phase for many aerospace applications. In Ocokoljića *et al.* (2017), for example, a similar procedure of deriving correlations from limited experimental and vast numerical data is evaluated for an actively controlled ballistic missile. In Mouton *et al.* (2012), CFD models are used to extrapolate wind tunnel data for a light aircraft, and data-reduction and comparison procedures are presented to create a combined model using both data sets.

In order to work with both data sets, it is first important to define some important quantities of interest. The coefficient of pressure (C_p, Eq. 1) is a standard non-dimensional representation of the total pressure (p) divided by the dynamic pressure (ρU_∞^2), where ρ is the air's density (taken as a constant value for low apogee rockets) and U_∞ is the air freestream's speed. p_∞ is a reference pressure value for the freestream, being equal to the standard atmospheric air pressure at sea level in this work.

$$C_p = \frac{2\,(p - p_\infty)}{\rho U_\infty^2} \tag{1}$$

The coefficient of pressure uses p_∞ as a reference pressure value. However, as previously discussed, the differential pressure transducer setup proposed in this work captures the pressure difference between the measurement lines along the rocket's nosecone. Therefore, a new non-dimensional quantity is proposed here, the coefficient of differential pressure (C_h, Eq. 3). C_h is computed using H (Eq. 2) as a pressure difference, instead of $(p - p_\infty)$ used in Eq. 1 . In Eq. 2, the *i-th* H pressure difference value is computed as the sum of the magnitudes of Δp between lines A, B and C for the *i-th*

pressure tap orifice.

$$H_i = |p_{A,i} - p_{B,i}| + |p_{A,i} - p_{C,i}| + |p_{B,i} - p_{C,i}| \tag{2}$$

$$C_{h_i} = \frac{2H_i}{\rho U_\infty^2} \tag{3}$$

C_h is a valuable coefficient for the transfer model, as it can be completely measured in real time during flight; with H values being acquired by the micro electronic differential pressure transducers and U_∞ values being estimated by regular IMU chip-sets already present in the rocket's avionics. Moreover, C_h is expected to present minimal variations with M_a, since it is non-dimensionalized by the dynamic pressure. C_h can also be understood as ΔC_p between lines A, B and C; given that if the H coefficient were defined with values of C_p than the terms containing p_∞ would be canceled.

The transfer model correlating C_h and α follows the general form of Eq. 4, where $\overline{\alpha}$ relates to the mean prediction of the model, and $\tilde{\alpha}$ is a fluctuating term modeling the prediction uncertainties.

$$\alpha(C_h) = \overline{\alpha}(C_h) \pm \tilde{\alpha}(C_h) \tag{4}$$

The CFD-obtained results were used as the basis of the transfer model, defining its overall tendency ($\overline{\alpha}$). This was done because the numerical results spanned a greater range of α and M_a conditions. Furthermore, the CFD simulations also included negative α scenarios. This is important given that the rocket's rotation is hard to measure or quantify during flight. With a range of results spanning both $\alpha < 0$ and $\alpha > 0$, the CFD simulations could define a bounded space correlating C_h and α, wherein the results for all other rotations of the rocket would theoretically lie. With this approach, the output α of the transfer model could be interpreted as $|\alpha|$, that is, by ignoring the rocket's rotation and dealing with absolute values of α, the model is capable of predicting absolute deviations of the rocket from its nominal flight path. Following these considerations, the mean tendency of the predicted angle of attack ($\overline{\alpha}$) was estimated as the quadratic regression of the CFD results.

The experimental results were used to quantify the transfer model uncertainties, included in the transfer model as a fluctuating angle of attack term ($\tilde{\alpha}$), also dependent on the input of C_h. This was done by first evaluating the individual measurement uncertainties associated with the water column manometer and the differential pressure transducer, and then comparing the linear tendencies of each measurement method. This method provides a crude estimate of the uncertainties, but it can be sufficient in determining a conservative range of validity for the angle of attack measurement system.

$$\tilde{\alpha}(C_h) = \frac{1}{2}\left[|r_m(C_h) - r_s(C_h)| + \Lambda_m + \Lambda_s|_\alpha\right] \tag{5}$$

The constant measurement uncertainty of the manometer (Λ_m) was simply defined by its measuring scale of 1mm, also considering its inclination of $60°$. This value was very small in magnitude when compared with the other uncertainties included in the transfer model. The uncertainty of the sensor measurement ($\Lambda_s|_\alpha$) was taken as the standard deviation of the measured signal for each value of α. The manometer and sensor results were fitted by the linear regressions $r_m(C_h)$ and $r_s(C_h)$, respectively, and the magnitude of the difference between these two lines was also included in the final model uncertainty ($\tilde{\alpha}$, Eq. 5). The uncertainty parameters discussed here can be clearly observed in Fig. 8.

3. RESULTS AND DISCUSSION

Figure 6 illustrates the distribution of the coefficient of pressure (C_p) along the dimensionless nosecone length x/l_n, where l_n is the total length of the nosecone. The experimental results obtained by the water column manometer are displayed for each of the ten pressure taps located along measurement lines A, B and C. CFD results are displayed as continuous lines. The C_p manometer data error-bars are too small to be discernible (on the order of 1e-3), and were therefore omitted from Fig 6. The CFD results capture an expected asymptotic tendency at the nosecone's tip, an effect which the manometer results naturally cannot capture given the absence of pressure taps at the very beginning of the nosecone's profile. Figure 6 is limited in its y-axis to facilitate the visualization of the experimental results, and the cut-off curve of the $C_{p,A}$ CFD results presents the same asymptotic tendency as curves $C_{p,B}$ and $C_{p,C}$.

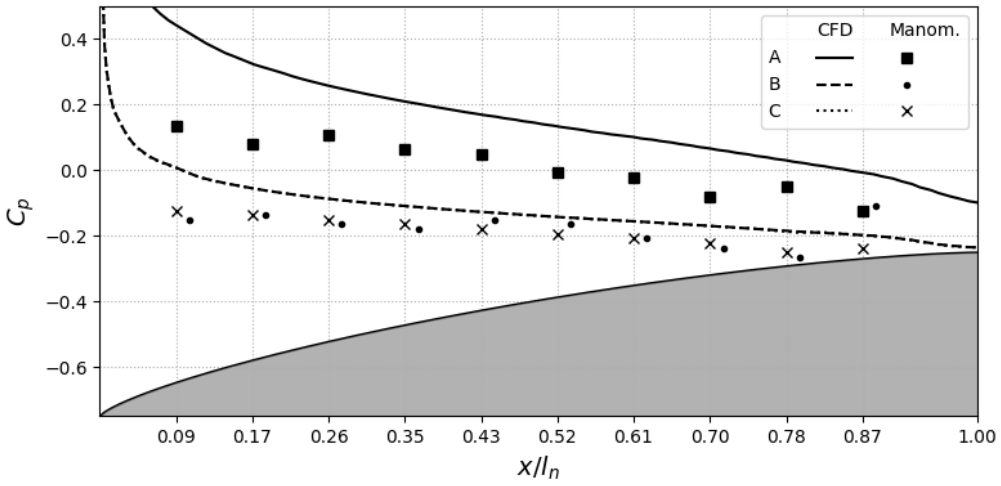

Figure 6: C_p distribution along the nosecone for $M_a = 0.08$, $\alpha = 10°$. The asymmetric x-grading of the plot corresponds exactly to the location of the ten pressure taps. The lower shaded region of the plot is an illustration of the Von Kármán profile of the Armação rocket's nosecone. The manometer results for line B were slightly shifted for ease of visualization.

Figures 7a and 7b illustrate the distributed coefficient of pressure field at the rocket's nosecone surface calculated by the incompressible CFD model. The simulations shown were carried out for speeds of 26.2 m/s ($M_a = 0.08$) and for positive angles of attack of 2.5° and 10°, in order to illustrate the evolution of the C_p field with α. Views normal to measurement lines A (Fig 7a) and B (Fig. 7b) are shown to highlight the potential differential pressure measurements that could be obtained by the proposed α measurement system. Results for line C are symmetrical to those of line B. The location of the surface pressure probes (corresponding to the pressure taps in the model nosecone) can also be seen in the aforementioned figures.

With the visualization of the pressure fields it is clear to notice that larger pressure gradients between lines A, B and C occur nearer to the nosecone's tip, as expected. This indicates that larger values of C_h can be expected to be measured by the pressure probes located in the nosecone's fore section. On the other hand, at the nosecone's far end, the pressure gradients become smaller and less distinct, indicating that differential pressure measurements at these locations could be harder.

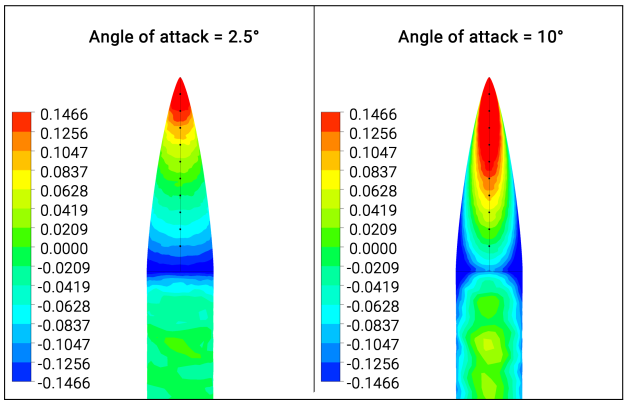

(a) C_p field on line A.

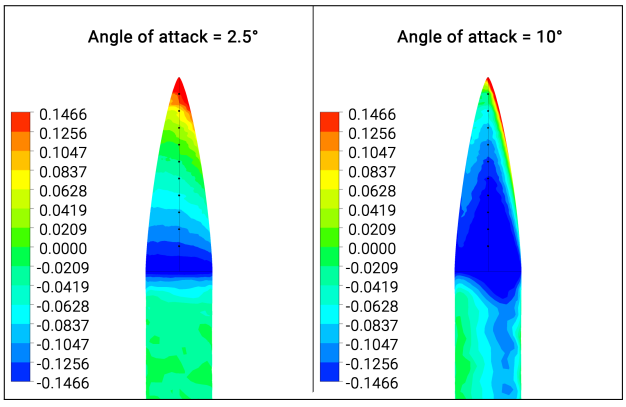

(b) C_p field on line B.

Figure 7: Total coefficient of pressure fields obtained by the CFD model for $M_a = 0.08$ and $\alpha = [2.5°, 10°]$. The C_p scale is capped off at values equivalent to total relative pressures of ± 50 Pa, in order to enlarge the regions with grater amplitudes of C_p.

Figure 8 presents the wind tunnel results for the tests carried out with simultaneous measurements of the water column manometer and the differential pressure transducer. Both the measured results and their best-fit linear regressions are included in Fig. 8, pertaining to values measured at the third and ninth pressure taps.

Many noteworthy conclusions can be drawn from the exposed results. Firstly, larger values of C_h were indeed obtained nearer to the nosecone's tip (pressure tap #3), as the CFD values predicted. Secondly, a distinct systematic error can be observed for the tests at $\alpha = 0°$, were C_h values of zero were to be expected, given the axisymmetric flow conditions at this angle of attack. The non-zero value of C_h can be attributed to a potential misalignment of the model nosecone within the wind tunnel, as discussed in Coutinho Coutinho (2021). Thirdly, a considerable measurement uncertainty (derived

from the signal's standard deviation during the measurement window) can be observed for the differential pressure sensor, indicating that the measured signal was excessively noisy. Coutinho Coutinho (2021) argues that this could be due to the small magnitudes of the local pressure measurement, which were on the same order as the sensor sensitivity (of approximately 0.1 kpa). If this hypothesis proves to be correct, then more consistent sensor measurements can be expected at higher M_a values.

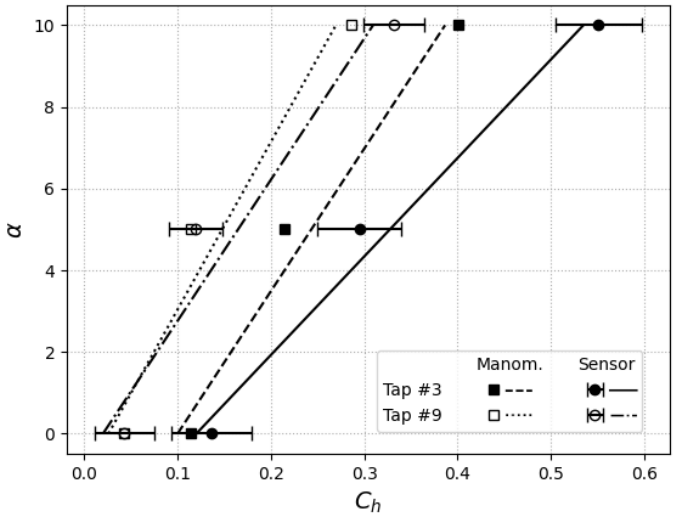

Figure 8: Experimental results. Lines represent the linear regressions of the data points. Error bars of the manometer values were omitted since they are too small to be distinguishable.

Finally, a distinct divergence between the linear regressions of the baseline manometer measurements and the micro electronic differential pressure sensor measurements can be observed in Figure 8. This divergence appears to be more pronounced for the higher pressure gradients measured at the third pressure tap, but is also noted for the ninth pressure tap measurements. As discussed in Sec. 2.3, the estimated uncertainty in the transfer model included the difference between the linear regressions of the experimental results as one of its principal terms (in the calculation of $\tilde{\alpha}$, Eq. 5). The observed divergence between the values measured by the manometer and the differential pressure sensor will therefore lead to increasingly uncertain predictions of α for higher inputs of measured C_h values.

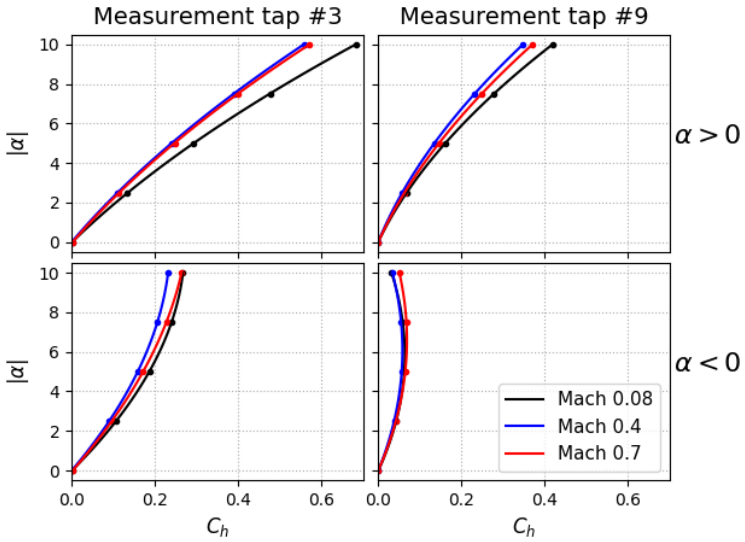

Figure 9: Numerical results. The legend present in the lower right plot is valid for the entire figure. All plots follow the same grading scale.

Figure 9 presents the results of the pressure probe readings obtained through the CFD simulations, divided between the third and ninth pressure taps, and for positive and negative angles of attack. The results are plotted for absolute magnitudes of α. This was done since the rocket's rotation is being ignored in this work, and the principal concern of the proposed measurement system and transfer model is to quantify how much and how frequently the rocket has deviated

from nominal flight conditions. The quadratic regression of these results was used to estimate the mean tendency of the proposed transfer model ($\overline{\alpha}$ term in Eq. 4).

Once again, larger values of C_h resulting from higher pressure gradients are observed for the results of the third pressure tap, as was also apparent in Fig. 8. The numerical results, however, do not show the systematic error at $\alpha = 0°$ that were observed in the wind tunnel experiments. Another notable similarity between the numerical and experimental data sets is the overall tendency of the $\alpha > 0$ results, with a clear, well-behaved, quadratic functional relationship being observed between C_h and α, which can be noted even for the small sample points of Fig. 8. On the other hand, for the CFD cases with $\alpha < 0$, this functional relationship becomes invalid, especially for the values obtained at the ninth pressure tap.

The inclusion of the $\alpha < 0$ cases in the CFD analysis shows that is not recommended to install the differential pressure sensor on the nosecone's aft section. Even though the experimental measurements with the differential pressure sensors located at the ninth pressure tap had a lesser systematic error and led to a lower overall model estimated uncertainty, the breakdown of the functional relationship between C_h and α observed for the lower right plot of Fig. 9 invalidates this option.

Figure 10 illustrates the final transfer model for α, using the mean predictions ($\overline{\alpha}$) obtained by the CFD models and the uncertainty term ($\tilde{\alpha}$) from the experimental results for the third pressure tap scenario. The curves of $\overline{\alpha}$ represent the quadratic regression of the CFD results, and the shaded region denoting $\tilde{\alpha}$ was calculated following Eq. 5. The $\overline{\alpha}$ values defined for the $\alpha < 0$ and $\alpha > 0$ cases form a bounded region containing all possible intermediary rocket rotation results.

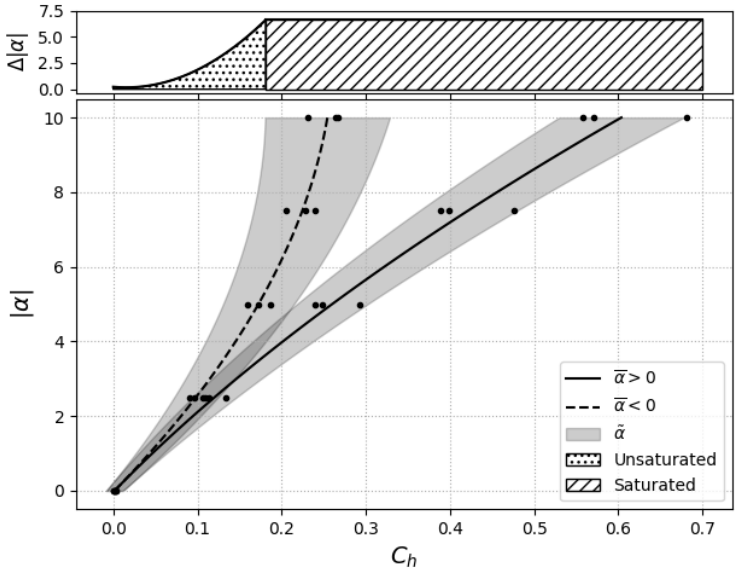

Figure 10: Final transfer model correlating a measured input of C_h with an estimated output of α. The unlabeled dots correspond to the CFD results for the third pressure tap and for all M_a values in Fig. 9. The upper auxiliary axis indicates the range of validity of the model's α predictions for any given input of C_h.

An auxiliary plot is also provided in Fig. 10 to represent the range of angle of attacks ($\Delta|\alpha|$) that can be predicted as an output given the same input of C_h. It is clear that the model becomes undetermined (or saturated) for values of $C_h > 0.18$. After this point, the mean tendency of the negative angle of attack CFD results ($\overline{\alpha} < 0$) tends asymptotically upwards, leading to larger values of $\Delta|\alpha|$.

This behavior strongly indicates that the proposed transfer model is only adequate in predicting small amplitudes of variation in the rocket's angle of attack. To avoid arriving at undefined outputs, a proposed solution could be saturating the transfer model output at $\alpha = 5°$. This condition is, however, not as discouraging as it may seem, given that prominent model rocketry literature (Mandell, 1968-1969) indicates that α oscillations with an amplitude greater than $2°$ are not typical in straight level flights, and could therefore be used to indicate that the rocket has indeed deviated from nominal flight conditions.

4. CONCLUSIONS

This work proposed an in-flight angle of attack measurement system to be used as a payload in low apogee high power model rockets. A brief description of the α measurement system architecture using a micro electronic differential pressure transducer was given. Experimental subsonic wind tunnel tests were conducted to acquire water column manometer baseline data for validating the sensor system's architecture.

Compressible and incompressible CFD models were constructed for the rocket in free flight conditions at varied angles

of attack (α) and Mach numbers (M_a). The numerical results showed good agreement with the baseline experimental measurements. A transfer model correlating α with the in-flight measured coefficient of differential pressure (C_h) was created by combining the mean tendency of the numerical results with an conservative estimate of the model uncertainty derived from the experimental results.

Finally, the transfer model was found to be adequately defined for C_h values up to 0.18, predicting coherent values of α for angles below $5°$, at which point the model is deemed to be saturated. This result can prove to be valuable in determining how often and in which conditions the rocket deviates from nominal flight conditions ($\alpha < 2°$).

5. REFERENCES

Avelar, A.C., Falc, J., Hsu, J.J.L., Basso, E. and Romero, P.G.M., 2014. *Experimental and Numerical Analysis of the Flow Patterns Around a Sounding Rocket in the Transonic Regime*. doi:10.2514/6.2014-3136. URL `https://arc.aiaa.org/doi/abs/10.2514/6.2014-3136`.

Barrowman, J.S. and Barrowman, J.A., 1966. "The theoretical prediction of the center of pressure". Available at http://www.nar.org/wp-content/uploads/2016/01/barrowman$_c p_e xtended_e dition.pdf$. Accessed 07 August 2021.

Box, S., Bishop, C. and Hunt, H., 2010. "A stochastic six-degree-of-freedom flight simulator for passively controlled high power rockets". *Journal of Aerospace Engineering - J AEROSP ENG*, Vol. 24. doi:10.1061/(ASCE)AS.1943-5525.0000051.

Coutinho, B.H., 2021. *Aerodynamic analysis and testing of dynamic pressure field at a rocket's nosecone surface*. Master's thesis, Graduate Program in Mechanical Engineering, Federal University of Santa Catarina, Florianópolis, Brasil.

Goetten, F., Finger, D.F., Marino, M., Bil, C., Havermann, M. and Braun, C., 2019. "A review of guidelines and best practices for subsonic aerodynamic simulations using rans cfd". In *Proceedings Of The Asia Pacific International Symposium On Aerospace Technology - APISAT 2019*.

Honório, H.T. and Maliska, C.R., 2014. "On the performance of coupled and segregated methods for solving two-dimensional incompressible flows employing unstructured grids". In *Proceedings of the 15th Brazilian Congress of Thermal Sciences and Engineering - ENCIT 2014*. Belém, PA, Brazi.

Mandell, G.K., 1968-1969. "Model rocketry magazine: Fundamentals of dynamic stability". Available at https://www.nar.org/members/magazine-archives/model-rocketry-magazine/. Accessed 12 April 2021.

Menter, F.R., Kuntz, M. and Langtry, R., 2003. "Ten years of industrial experience with the sst turbulence model". *Turbulence, Heat and Mass Transfer*, Vol. 4.

Mitchell, J.L. and Peck, R.F., 1955. "An naca vane-type angle-of-attack indicator for use at subsonic and supersonic speeds". Available at https://ntrs.nasa.gov/citations/19930084339. Accessed 07 August 2021.

Mouton, S., Rantet, E., Gouverneur, G. and Verbeke, C., 2012. "Combined wind tunnel tests and flow simulations for light aircraft performance prediction". In *Proceedings of the 47th International Symposium of Applied Aerodynamics*. Paris, France.

Mueller, T.R., Vogt, D.M., Fischer, M. and Phillipsen, B.A., 2020. "On the far-field boundary condition treatment in the framework of aeromechanical computations using ansys cfx". In *Institution of Mechanical Engineers, Part A: Journal of Power and Energy*.

Nakakita, K., Takama, Y., Imagawa, K. and Kato, H., 2012. *Unsteady PSP Measurement of Transonic Unsteady Flow Field around a Rocket Fairing Model*. doi:10.2514/6.2012-2758. URL `https://arc.aiaa.org/doi/abs/10.2514/6.2012-2758`.

Nakos, D., 2013. *High resolution schemes for bluff–body aerodynamics*. Master's thesis, School of Engineering, Department of Engineering Physics, Cranfield University, Cranfield, United Kingdom.

NXP, 2017. *MPXV7002 Integrated Silicon Pressure Sensor On-Chip Signal Conditioned, Temperature Compensated and Calibrated*. NXP Semiconductors, Data Sheet.

Ocokoljića, G.J., Rašuob, B.P. and Benginb, A., 2017. "Aerodynamic shape optimization of guided missile based on wind tunnel testing and cfd simulation". *Thermal Science*, Vol. 21.

Pavliuchenko, A., Shyiko, O. and Klochkova, T., 2020. "Measurement of the angle of attack of an aerophysical missile complex in flight based on the hall effect sensor and electronic measurement system". *Journal of Nano- and Electronic Physics*, Vol. 12, No. 4, p. 5. doi:https://doi.org/10.21272/jnep.12(4).04025.

Spalart, P.R. and Allmaras, S.R., 1992. "A one-equation turbulence model for aerodynamic flows". *AIAA*, Vol. 30.

Zore, K., Parkhi, G., Sasanapuri, B. and Varghese, A., 2019. "Ansys mosaic poly-hexcore mesh for high-lift aircraft configuration". In *Proceedings of the 21st Annual CFD Symposium*. Bangalore, India.

6. RESPONSIBILITY NOTICE

The authors are solely responsible for the printed material included in this paper.